High-Resolution Upwind Schemes for the Three-Dimensional Incompressible Navier-Stokes Equations

Peter-M. Hartwich* and Chung-Hao Hsu†
Vigyan Research Associates, Inc., Hampton, Virginia

Based on flux-difference splitting, implicit high-resolution schemes are constructed for efficient computations of steady-state solution to the three-dimensional, incompressible Navier-Stokes equations in curvilinear coordinates. These schemes use first-order-accurate Euler backward-time differencing and second-order central differencing for the viscous shear fluxes. Up to third-order-accurate upwind differencing is achieved through a reconstruction of the solution from its cell averages. The reconstruction is accomplished by linear interpolation, where the node stencils are selected such that in regions of smooth solution the flow is highly resolved while spurious oscillations in regions of rapid changes in gradient are still suppressed. Fairly rapid convergence to steady-state solutions is attained with a vectorizable hybrid time-marching method. Flows around a sharp-edged delta wing are computed with the maximum accuracy of the upwind differencing restricted to first, second, and third order, to illustrate the effect of accuracy on the global and on the local vortical flowfields. The results are validated with experimental data.

I. Introduction

THERE are basically two options to compute three-dimensional low-speed flows as steady-state solutions to the Navier-Stokes equations: numerical approximations 1) to the compressible Navier-Stokes equations for low Mach numbers (M), or 2) to the incompressible Navier-Stokes equations. In view of the numerous time-dependent methods, both explicit[1] and implicit,[2-4] for the compressible Navier-Stokes equations, the first option appears to be a viable choice. However, the efficiency of these schemes deteriorates considerably with decreasing subsonic Mach number due to the "stiffness" of the physical problems associated with low-speed, viscous flow. The stiffness arises from both disparate characteristic speeds and length scales. Furthermore, the accuracy of low-speed flowfield computations with implicit approximate factorization (AF) schemes (e.g., those in Refs. 2-4) becomes questionable for low Mach numbers, since the factorization errors increase in an unbounded fashion for a decreasing Mach number.[5] That suggests to remove the sound speed time scale and to assume the flow to be truly incompressible.

Aziz and Hellums[6] proposed to solve the Navier-Stokes equations for incompressible, fully three-dimensional flow in a vector potential-vorticity formulation. Because of its storage requirements and the necessity to solve three Poisson equations at each time level, that method failed to become popular. That leaves solving the Navier-Stokes equations for three-dimensional, incompressible flow in their primitive variable formulation. Common methods for this formulation advance the solution for the velocity field by explicitly or implicitly solving the equations of motion. The updated velocity field is used to compute the corresponding pressure field by solving a Poisson equation[7] or by an iterative procedure with the equation of continuity as a compatibility condition.[8] Such schemes were tried but abandoned for an implicit flux-difference splitting scheme applied to a system of first-order hyperbolic partial differential equations. The extension of this method to the incompressible Navier-Stokes equations is described in the next three sections. The new schemes are applied to compute vortical flows around a sharp-edged delta wing ($AR=1$, $t/c=0$) over a range of angles of attack. The purpose of these test calculations is 1) to demonstrate how the accuracy of the upwind differences affects the accuracy of the computed flowfield results, and 2) to validate the numerical results with experimental data.

II. Governing Equations

The Navier-Stokes equations in conservation law form for an incompressible, three-dimensional flow are written as

$$Q_t + (E^* - E_v^*)_x + (F^* - F_v^*)_y + (G^* - G_v^*)_z = 0 \tag{1}$$

with the inviscid flux vectors

$$E^* = (\beta u, u^2 + p, uv, uw)^T \tag{2a}$$

$$F^* = (\beta v, uv, v^2 + p, vw)^T \tag{2b}$$

$$G^* = (\beta w, uw, vw, w^2 + p)^T \tag{2c}$$

and the shear flux vectors

$$E_v^* = Re^{-1}(0, 2u_x, u_y + v_x, u_z + w_x)^T \tag{3a}$$

$$F_v^* = Re^{-1}(0, u_y + v_x, 2v_y, v_z + w_y)^T \tag{3b}$$

$$G_v^* = Re^{-1}(0, u_z + w_x, v_z + w_y, 2w_z)^T \tag{3c}$$

where $Re = \rho V_\infty L/\mu$. The Cartesian components u,v,w are scaled with the freestream velocity V_∞. The Cartesian coordinates x,y,z are normalized with some length, which is characteristic for a considered flow problem (here, $L=c$, the root chord of the delta wing). The nondimensional pressure is defined as $p=(P-P_\infty)/\rho V_\infty^2$. The molecular viscosity μ is assumed to be constant.

Chorin[9] suggested using artificial compressibility when solving the equation of continuity. That is comprised in Eq.

Presented as Paper 87-0547 at the AIAA 25th Aerospace Sciences Meeting, Reno, NV, Jan. 12-15, 1987; received April 24, 1987; revision received Jan. 15, 1988.

*Research Scientist. Member AIAA.
†Research Engineer. Senior Member AIAA.

(1) by defining the dependent variable vector $\boldsymbol{Q}$ as

$$\boldsymbol{Q}=(p,u,v,w)^T \tag{4}$$

which adds a time-derivative of the pressure to the continuity equation. This contrivance couples the equations of motion with the continuity equation. Then one can apply the most efficient implicit time-dependent methods to Eq. (1), i.e., those which solve the complete set of governing equations simultaneously (e.g., Warming and Beam[10] gave a clear account thereon). The coefficient β in Eqs. (2) monitors the amount of artificial compressibility, which diminishes for large values of β or when the solution of Eq. (1) approaches asymptotically a steady state. The choice of appropriate values of β for steady-state computations will be discussed shortly.

Considering a coordinate transformation of the form $\zeta=\zeta(x,y,z)$, $\xi=\xi(x,y,z)$, and $\eta=\eta(x,y,z)$, Eq. (1) is rewritten in strong conservation law form as

$$(\boldsymbol{Q}/J)_t+(\boldsymbol{E}-\boldsymbol{E}_v)_\zeta+(\boldsymbol{F}-\boldsymbol{F}_v)_\xi+(\boldsymbol{G}-\boldsymbol{G}_v)_\eta=0 \tag{5}$$

with

$$\begin{bmatrix}\boldsymbol{E}-\boldsymbol{E}_v\\ \boldsymbol{F}-\boldsymbol{F}_v\\ \boldsymbol{G}-\boldsymbol{G}_v\end{bmatrix}=\begin{bmatrix}\zeta_x/J & \zeta_y/J & \zeta_z/J\\ \xi_x/J & \xi_y/J & \xi_z/J\\ \eta_x/J & \eta_y/J & \eta_z/J\end{bmatrix}\begin{bmatrix}\boldsymbol{E}^*-\boldsymbol{E}_v^*\\ \boldsymbol{F}^*-\boldsymbol{F}_v^*\\ \boldsymbol{G}^*-\boldsymbol{G}_v^*\end{bmatrix} \tag{6}$$

where $U=a_1u+a_2v+a_3w$ is the contravariant velocity component, and $S=[U^2+\beta(a_1^2+a_2^2+a_3^2)]^{1/2}$. For large β, the condition number $|\lambda_{\max}|/|\lambda_{\min}|$ is large, and the system of partial differential equations is stiff. In order to avoid excessive values of β, Rizzi and Eriksson[11] proposed to choose β proportional to the dynamic pressure $u^2+v^2+w^2$ for inviscid flow. For viscous flow, extended regions with small dynamic pressure might occur (e.g., secondary vortices on delta wings). With $\beta\sim u^2+v^2+w^2$, the amount of artificial compressibility increases in those regions, too. This leads to an incompatibility in the governing equations that results in meaningless solutions (a steady-state solution to the Navier-Stokes equations has never been obtained with $\beta\sim u^2+v^2+w^2$). Choosing β to be 0(1) (or simply set it to unity) ensures that the condition number varies in the range between 0(1) and 0(10), which eliminates any stiffness-related convergence problems in computing asymptotic steady-state solutions to Eq. (5).

The relation between the Jacobian D and the eigenvalues in the diagonal matrix $\boldsymbol{\Lambda}$ is given by a similarity transformation $\boldsymbol{D}=\boldsymbol{R}\boldsymbol{\Lambda}\boldsymbol{R}^{-1}$. The columns of $\boldsymbol{R}$ are the right eigenvectors, and the rows of $\boldsymbol{R}^{-1}$ give an orthonormal set of left eigenvectors. The generalized formulation of $\boldsymbol{R}$ and $\boldsymbol{R}^{-1}$ reads

$$R=\begin{bmatrix}-\beta\hat{S} & \beta\hat{S} & 0 & 0\\ \hat{a}_1\beta+u\hat{\lambda}_1 & \hat{a}_1\beta+u\hat{\lambda}_2 & -\hat{a}_2 & -\hat{a}_3\\ \hat{a}_2\beta+v\hat{\lambda}_1 & \hat{a}_2\beta+v\hat{\lambda}_2 & \hat{a}_1+\hat{a}_3 & -\hat{a}_3\\ \hat{a}_3\beta+w\hat{\lambda}_1 & \hat{a}_3\beta+w\hat{\lambda}_2 & -\hat{a}_2 & \hat{a}_1+\hat{a}_2\end{bmatrix} \tag{11}$$

$$R^{-1}=\frac{1}{2\hat{S}^2}\begin{bmatrix}-\hat{\lambda}_2/\beta & \hat{a}_1 & \hat{a}_2 & \hat{a}_3\\ -\hat{\lambda}_1/\beta & \hat{a}_1 & \hat{a}_2 & \hat{a}_3\\ (\hat{\lambda}_2d_1+\hat{\lambda}_1d_2)/\beta & -2\hat{S}^2/k-\hat{a}_1d_5 & 2\hat{S}^2/k-\hat{a}_2d_5 & -\hat{a}_3d_5\\ (\hat{\lambda}_2d_3+\hat{\lambda}_1d_4)/\beta & -2\hat{S}^2/k-\hat{a}_1d_6 & -\hat{a}_2d_6 & 2\hat{S}^2/k-\hat{a}_3d_6\end{bmatrix} \tag{12}$$

The Cartesian derivatives in the shear fluxes are to be expanded in ζ, ξ, η space by chain rule such as $u_x=\zeta_xu_\zeta+\xi_xu_\xi+\eta_xu_\eta$, etc. The Jacobian of the coordinate transformation is given by

$$J^{-1}=x_\zeta(y_\xi z_\eta-y_\eta z_\xi)+x_\xi(y_\eta z_\zeta-y_\zeta z_\eta)+x_\eta(y_\zeta z_\xi-y_\xi z_\zeta) \tag{7}$$

The Jacobians of the inviscid fluxes $\boldsymbol{E},\boldsymbol{F},\boldsymbol{G}$ are needed for the flux-difference splitting and for the implicit algorithm to be defined later. The flux vectors $\boldsymbol{E},\boldsymbol{F},\boldsymbol{G}$ are all linear combinations of $\boldsymbol{E}^*$, $\boldsymbol{F}^*$, $\boldsymbol{G}^*$

$$\boldsymbol{H}=a_1\boldsymbol{E}^*+a_2\boldsymbol{F}^*+a_3\boldsymbol{G}^* \tag{8}$$

with $\boldsymbol{H}=\boldsymbol{E}$, $\boldsymbol{F}$, or $\boldsymbol{G}$, and $a_1=\zeta_x/J$, ξ_x/J, or η_x/J, etc., so that the Jacobian $\boldsymbol{D}=\partial\boldsymbol{H}/\partial\boldsymbol{Q}$ is given by

$$\boldsymbol{D}=a_1\boldsymbol{A}^*+a_2\boldsymbol{B}^*+a_3\boldsymbol{C}^* \tag{9}$$

where $\boldsymbol{D}=\boldsymbol{A}$, $\boldsymbol{B}$, or $\boldsymbol{C}$, and $\boldsymbol{A}=\partial\boldsymbol{E}/\partial\boldsymbol{Q}$, etc. The Jacobians $\boldsymbol{A}^*$, $\boldsymbol{B}^*$, $\boldsymbol{C}^*$ are formed from the Cartesian flux vectors like in Steger and Kutler.[5] The eigenvalues of $\boldsymbol{D}$ are

$$\boldsymbol{\Lambda}=\mathrm{diag}(\lambda_1,\lambda_2,\lambda_3,\lambda_4)=\mathrm{diag}(U-S,U+S,U,U) \tag{10}$$

where

$$k=\hat{a}_1+\hat{a}_2+\hat{a}_3$$

$$\hat{a}_1,\hat{a}_2,\hat{a}_3=a_1,a_2,a_3/(a_1^2+a_2^2+a_3^2)^{1/2}$$

$$d_1=(r_{31}-r_{21})/k, \qquad d_2=(r_{32}-r_{22})/k,$$

$$d_3=(r_{41}-r_{21})/k, \qquad d_4=(r_{42}-r_{22})/k,$$

$$d_5=d_1+d_2, \qquad d_6=d_3+d_4$$

Quantities like $r_{31}(=\hat{a}_2\beta+v\hat{\lambda}_1)$ indicate elements of R in Eq. (11), and $\hat{S}=S(u,v,w,\hat{a}_1,\hat{a}_2,\hat{a}_3)$, etc.

For the formulation of the implicit algorithm, the Jacobians of the shear fluxs $\boldsymbol{E}_v,\boldsymbol{F}_v,\boldsymbol{G}_v$ are also needed. As usual, these vectors are first simplified by neglecting all cross-derivative terms, and then they are linearized by Taylor series as in Pulliam and Steger.[2] That produces the coefficient matrices

$$X,\ Y \text{ or } Z=(Re^{-1}J)\,\mathrm{diag}(0,m_1,m_2,m_3) \tag{13}$$

with $m_1=2a_1^2+a_2^2+a_3^2$, $m_2=a_1^2+2a_2^2+a_3^2$, and $m_3=a_1^2+a_2^2+2a_3^2$. For example, to obtain Y, $\alpha_1=\xi_x/J$, $a_2=\xi_y/J$, and $a_3=\xi_z/J$.

III. Spatial Differencing

Taking the parabolic time-dependent Navier-Stokes equations in the limit of an infinite Reynolds number yields the hyperbolic time-dependent Euler equations. That suggests a spatial differencing that reflects the different type of the partial differential equations for a finite and an infinite Reynolds number: central differencing for the viscous fluxes and upwind differencing for the inviscid fluxes.

Upwind schemes possess an inherent solution-adaptive dissipation that alleviates the necessity to add and tune dissipative terms for numerical stability and accuracy as in schemes with central differencing. Their superior robustness comes at the expense of increased computional work in comparison to central-difference schemes. This shortcoming is partly offset because upwind differencing allows for the construction of implicit methods, which are simpler and/or faster than those devised with central-difference schemes.[12,13]

Discretization of the Inviscid Fluxes

The upwind differencing is implemented by adapting Roe's flux-difference splitting[14] to Eq. (5). Unlike other splitting methods, the flux-difference splitting maintains the strong conservation law form in Eq. (5). The flux vector splitting by Steger and Warming[12] only preserves a strong conservation law form of the governing equations of ideal gas flow, since it requires inviscid fluxes that are homogeneous of degree one in the dependent variable vector. The assumption of compressible flow is also crucial in Van Leer's flux vector splitting,[15] where the inviscid fluxes are expressed in terms of density, speed of sound, and Mach number. Split coefficient matrix methods[16] are applicable to the governing equations of compressible and incompressible flow, but they are derived for systems of partial differential equations in nondivergence form.

Common to all of these splitting methods is that they are devised for one-dimensional hyperbolic conservation laws. For multidimensional applications, the inviscid flux terms are generally treated independently in each coordinate direction and then added up. This approach is also adopted in this paper.

Consider a system of quasi one-dimensional, hyperbolic partial differential equations:

$$(\boldsymbol{Q}/J)_t + \boldsymbol{H}_\theta = 0 \tag{14}$$

where $\theta = \zeta$, ξ, or η. Defining computational cells with their centroids at $\ell = \theta/\Delta\theta$, ($\ell = i,j$, or k) and their cell interfaces at $\ell \pm \frac{1}{2}$, an implicit discrete approximation to Eq. (14) is written as

$$[(I/\tau J) + D_\ell \Delta_\ell]\Delta\boldsymbol{Q}^n + \Delta_\ell \boldsymbol{H}^n = 0 \tag{15}$$

where τ = time step, $\Delta Q^n = Q^{n+1} - Q^n$, and $\Delta_\ell(\ ) = [(\ )_{\ell+\frac{1}{2}} - (\ )_{\ell-\frac{1}{2}}]/\Delta\theta$. Equation (15) gives an Euler-implicit time differencing of first-order accuracy, which suffices for steady-state calculations. Let Q_ℓ and $Q_{\ell+1}$ denote two piecewise constant states of a Riemann initial value problem (IVP). These states are separated by one or more wave families. For compressible flow, there are genuinely nonlinear waves (shocks, rarefactions) and linearly degenerate waves (contact discontinuities).[17] The speed of the right or left traveling waves is given by the positive or negative eigenvalues of the matrix $\boldsymbol{D}$, respectively. For the construction of an approximate Riemann solver for the IVP in Eq. (15), it is useful to redefine the flux $\boldsymbol{H}$ at the point $\ell + \frac{1}{2}$ that separates the right from the left traveling waves.[13]

$$H^n_{\ell+\frac{1}{2}} = H^n_\ell + (\Delta H^-_{\ell+\frac{1}{2}})^n = H^n_{\ell+1} - (\Delta H^+_{\ell+\frac{1}{2}})^n \tag{16}$$

Upon inserting Eq. (16), Eq. (15) assumes

$$[(I/\tau J) + D_\ell \Delta_\ell]\Delta\boldsymbol{Q}^n + (\Delta H^-_{\ell+\frac{1}{2}} + \Delta H^+_{\ell-\frac{1}{2}})^n = 0 \tag{17}$$

Following Roe,[14] a mean value matrix $\boldsymbol{D}_{\ell+\frac{1}{2}} = \boldsymbol{D}(\boldsymbol{Q}_\ell, \boldsymbol{Q}_{\ell+1})$ is introduced with

$$\boldsymbol{D}_{\ell+\frac{1}{2}} \Delta_{\ell+\frac{1}{2}} \boldsymbol{Q} = \Delta \boldsymbol{H}_{\ell+\frac{1}{2}} \tag{18a}$$

$$\boldsymbol{D}(\boldsymbol{Q}_\ell, \boldsymbol{Q}_\ell) = \boldsymbol{D}_\ell \tag{18b}$$

which allows Eq. (17) to be written as

$$[(I/\tau J) - (\boldsymbol{D}^-_{\ell+\frac{1}{2}})^n \Delta_{\ell+\frac{1}{2}} + (\boldsymbol{D}^+_{\ell-\frac{1}{2}})^n \Delta_{\ell-\frac{1}{2}}]\Delta\boldsymbol{Q}^n$$
$$= (\boldsymbol{D}^-_{\ell+\frac{1}{2}})^n \Delta_{\ell+\frac{1}{2}} \boldsymbol{Q}^n - (\boldsymbol{D}^+_{\ell-\frac{1}{2}})^n \Delta_{\ell-\frac{1}{2}} \boldsymbol{Q}^n \tag{19}$$

where

$$\boldsymbol{D}^n_{\ell\pm\frac{1}{2}} = [\boldsymbol{R}(\boldsymbol{\Lambda}^+ - \boldsymbol{\Lambda}^-)\boldsymbol{R}^{-1}]^n_{\ell\pm\frac{1}{2}} = (\boldsymbol{D}^+ - \boldsymbol{D}^-)^n_{\ell\pm\frac{1}{2}} \tag{20}$$

with $\boldsymbol{\Lambda}^\pm = (|\boldsymbol{\Lambda}| \pm \boldsymbol{\Lambda})/2$. Because of the condition in Eq. (18a), the solution to Eq. (19) is conservative in space. It also approximates the same IVP as in Eq. (17), for the eigenvalues of $\boldsymbol{D}^n_{\ell\pm\frac{1}{2}}$ represent the wave speeds of the IVP in Eq. (17) due to Eq. (18b). The structure of $\boldsymbol{D}^n_{\ell\pm\frac{1}{2}}$ is identical with that of $\boldsymbol{D}$ and is found in Eqs. (9–12). Equation (18a) is identically fulfilled when $\boldsymbol{D}^n_{\ell+\frac{1}{2}} = \boldsymbol{D}(\boldsymbol{Q}^n_{\ell+\frac{1}{2}})$ where $\boldsymbol{Q}^n_{\ell+\frac{1}{2}} = (\boldsymbol{Q}^n_\ell + \boldsymbol{Q}^n_{\ell+1})/2$. In order to prevent the matrix in Eq. (12) from becoming singular, the metrics in $\boldsymbol{D}^n_{\ell+\frac{1}{2}}$ are computed from arithmetic averages of their values at their neighboring centroids, where they are differenced using a weighted average procedure.[2,13] For example,

$$(\xi_x/J)_{ijk} = [(\sigma_k \delta_j y)(\sigma_j \delta_k z) - (\sigma_j \delta_k y)(\sigma_k \delta_j z)]_i \tag{21}$$

where, for instance, the averaging operator σ_k working on $\Delta_j y$ is defined as

$$\sigma_k \delta_j y = [(\delta_j y)_{k+1} + (\delta_j y)_{k-1}]/2 \tag{22}$$

with $\delta_j(\ ) = [(\ )_{j+1} - (\ )_{j-1}]/2$.

This special averaging procedure brings the present finite-difference formulation close to a finite-volume method. It ensures that the flux differences taken over the six bounding surfaces $(i \pm \frac{1}{2}, j, k)$, $(i, j \pm \frac{1}{2}, k)$, and $(i, j, k \pm \frac{1}{2})$ of a three-dimensional cell at i,j,k cancel completely out for shear flows with constant gradients.

High-Resolution Schemes

For the construction of the scheme in Eq. (19), the states $\boldsymbol{Q}_\ell$ have been assumed to be constant across each computational cell. This is equivalent to replace the actual function $\boldsymbol{Q}(\theta)$ with its cell averages. When $\boldsymbol{Q}(\theta)$ is smooth (i.e., differentiable), the jumps $\Delta_{\ell\pm\frac{1}{2}}\boldsymbol{Q}$ in Eq. (19) are first-order accurate, one-sided difference approximations to $\partial\boldsymbol{Q}/\partial\theta\,|_{\ell\pm\frac{1}{2}}$. This contaminates the solutions of Eq. (19) with a considerable amount of numerical dissipation and smears the details of the actual solution to Eq. (14). Van Leer[18] pointed out that this accuracy problem stems from the replacement of $\boldsymbol{Q}(\theta)$ by its cell averages, which discards valuable information about $\boldsymbol{Q}(\theta)$. To recover that information, $\boldsymbol{Q}(\theta)$ is reconstructed from its cell averages $\boldsymbol{Q}_\ell$. The reconstruction is accomplished by linear interpolation where the node stencils are selected such that the solution is highly resolved in regions of smooth $\boldsymbol{Q}(\theta)$, while spurious oscillations are suppressed in regions of rapid changes of gradient. Such schemes are labeled high-resolution schemes as opposed to total variation diminishing (TVD) schemes, which completely eliminate any of those spurious oscillations when applied to one-dimensional nonlinear hyperbolic conservation laws and linear hyperbolic systems.[19–22]

Here, high-resolution schemes are presented that are accurate up to third order. The algorithms describing the nonlinear reconstruction process are taken from recently developed implicit, one-dimensional TVD schemes. For the nonlinear systems case, a TVD scheme cannot be constructed because no

quantity is known that is subject to a TVD requirement.[19,20] For a linear system case, the total variation (TV) of the characteristic variables $\boldsymbol{W} = \boldsymbol{R}^{-1}\boldsymbol{Q}$ can be forced to diminish in time. Assuming $\boldsymbol{R}$, $\boldsymbol{R}^{-1}$, and Λ to be constant, and using the definition for the characteristic variables, the scheme in Eq. (19) is rewritten as

$$[(1/\tau J) \pm \lambda_m^{\pm} \Delta_{\ell \mp \frac{1}{2}}] \Delta w_m^n = \mp \lambda_m^{\pm} \Delta_{\ell \mp \frac{1}{2}} w_m^n \tag{23}$$

where $m = 1,2,3,4$. Equation (23) comprises four scalar linear hyperbolic conservation laws. The scheme in Eq. (23) is unconditionally TVD.[20] To enhance the accuracy of Eq. (23) to up to third order, the values of w_w^n at the cell interfaces are reconstructed by using piecewise linear distributions:

$$w(\theta_{\ell \pm \frac{1}{2}}^{\pm}) = w_{m,\ell}^n \pm 0.25[(1+\omega)\phi_{m,\ell\pm1}^{\mp} \Delta_{\ell\pm\frac{1}{2}} w_m^n + (1-\omega)\phi_{m,\ell}^{\mp} \Delta_{\ell\mp\frac{1}{2}} w_m^n] \tag{24a}$$

$$w(\theta_{\ell \mp \frac{1}{2}}^{\pm}) = w_{m,\ell\mp1}^n \pm 0.25[(1+\omega)\phi_{m,\ell}^{\pm} \Delta_{\ell\pm\frac{1}{2}} w_m^n + (1-\omega)\phi_{m,\ell\mp1}^{\pm} \Delta_{\ell\mp\frac{1}{2}} w_m^n] \tag{24b}$$

with

$$\phi_{m,\ell}^{\pm} = \phi(r_{m,\ell}^{\pm}) \tag{24c}$$

and

$$r_{m,\ell}^{\pm} = \begin{cases} (\Delta_{\ell-\frac{1}{2}} w_m^n / \Delta_{\ell+\frac{1}{2}} w_m^n)^{\pm 1} & \text{for } \Delta_{\ell\pm\frac{1}{2}} w_m^n \neq 0 \\ 0 & \text{for } \Delta_{\ell\pm\frac{1}{2}} w_m^n = 0 \end{cases} \tag{24d}$$

where $\theta_{\ell+\frac{1}{2}}^{+}$ ($\theta_{\ell+\frac{1}{2}}^{-}$) is the limit from the left (right) at the cell interface at $\ell+\frac{1}{2}$. Inserting Eqs. (24) into Eq. (23) yields a family of new implicit TVD schemes:

$$\begin{aligned}[(1/\tau J) &\pm \lambda_m^{\pm} \Delta_{\ell\mp\frac{1}{2}})] \Delta w_m^n \\ &= \{\lambda_m^- - [(1-\omega)\lambda_m^- + (1+\omega)\lambda_m^+] \\ &\times (\phi_{m,\ell+1}^- - \phi_{m,\ell}^+)/4\} \Delta_{\ell+\frac{1}{2}} w_m^n \\ &- \{\lambda_m^+ + [(1-\omega)\lambda_m^+ + (1+\omega)\lambda_m^-] \\ &\times (\phi_{m,\ell}^- - \phi_{m,\ell-1}^+)/4\} \Delta_{\ell-\frac{1}{2}} w_m^n \end{aligned} \tag{25}$$

Note that the reconstruction applies only to the right-hand side of Eq. (25). The left-hand side of Eq. (25) cannot be reconstructed because that requires beforehand knowledge of w_m^{n+1}, which is simply not available. The non-TVD or unlimited forms of Eq. (25) are obtained by setting $\phi_{m,\ell}^{\mp} = 1$ and $\phi_{m,\ell}^{\pm} = r_{m,\ell}^{\pm}$ for $\lambda_m \gtrless 0$. The truncation error (TE) of the unlimited form is

$$\mathrm{TE} = 0.25(1/3 - \omega)(\Delta\theta)^2 (\partial^3 w_m / \partial\theta^3)$$

For example, for $\omega = -1$, the spatial derivatives in the non-TVD form are approximated by second-order-accurate, one-sided differences; for $\omega = 1/3$, by third-order-accurate, upwind-biased differences.

To determine the constraints on $\phi_{m,\ell}^{\pm}$ such that the new schemes are TVD, assume without any real loss in generality $\lambda_m > 0$, and write the implicit TVD scheme in Eq. (25) at location ℓ and $\ell+1$ as

$$\begin{aligned} &\Delta w_{m,\ell}^n + CFL_m^+ \Delta_{\ell-\frac{1}{2}} w_m^{n+1} + (CFL_m^+/4) \\ &\times [(1+\omega)(\phi_{m,\ell}^+ - \phi_{m,\ell+1}^-) + r_{m,\ell}^+ (1-\omega) \\ &\times (\phi_{m,\ell}^- - \phi_{m,\ell-1}^+)] \Delta_{\ell+\frac{1}{2}} w_m^n = 0 \end{aligned} \tag{26}$$

$$\begin{aligned} &\Delta w_{m,\ell+1}^n + CFL_m^+ \Delta_{\ell+\frac{1}{2}} w_m^{n+1} + (CFL_m^+/4) \\ &\times [(1-\omega)(\phi_{m,\ell+1}^- - \phi_{m,\ell}^+) + r_{m,\ell}^- (1+\omega) \\ &\times (\phi_{m,\ell+1}^+ - \phi_{m,\ell+2}^-)] \Delta_{\ell+\frac{1}{2}} w_m^n = 0 \end{aligned} \tag{27}$$

where $CFL_m^+ = \lambda_m^+ \tau J$. Subtracting Eq. (26) from Eq. (27), assuming b_1, b_2, $b_3 > 0$, and using the triangle inequality yields

$$b_1 |\Delta_{\ell+\frac{1}{2}} w_m^{n+1}| \leq b_2 |\Delta_{\ell-\frac{1}{2}} w_m^n| + b_3 |\Delta_{\ell+\frac{1}{2}} w_m^n| \tag{28}$$

with

$$\begin{aligned} b_1 &= 1 + CFL_m^+, \qquad b_2 = CFL_m^+ \\ b_3 &= 1 + (CFL_m^+/4)[2\omega(\phi_{m,\ell}^+ - \phi_{m,\ell+1}^-) \\ &\quad - (1+\omega) r_{m,\ell+1}^- (\phi^+{}_{m,\ell+1} - \phi_{m,\ell+2}^-) \\ &\quad + (1-\omega) r_{m,\ell}^+ (\phi_{m,\ell}^- - \phi_{\mathrm{m},\ell-1}^+)] \end{aligned}$$

If $w(\theta)$ is of compact support or periodic, and if $\phi(r_{m,\ell}^{\pm}) = 0$ for $r_{m,\ell}^{\pm} \leq 0$, the summation of Eq. (28) over all ℓ with $-\infty < \ell < \infty$ yields $\mathrm{TV}^{n+1} \leq \mathrm{TV}^n$ with

$$\mathrm{TV}^n := \sum_{-\infty}^{+\infty} |\Delta_{\ell+\frac{1}{2}} w_m^n|$$

which says that the TV diminishes with time. It is evident that $b_1, b_2 > 0$, but $b_3 > 0$ is only satisfied if

$$\phi_{m,\ell}^{\pm} = \max[0, 2 \cdot \min(1, r_{m,\ell}^{\pm}, \kappa \cdot r_{m,\ell\pm1}^{\mp})] \tag{29}$$

Equation (29) with $\kappa = 1$ is the constraint on $\phi_{m,\ell}^{\pm}$, which makes the new implicit, nonlinear schemes TVD. This result is obtained by evaluating $b_3 > 0$ for $-1 \leq \omega \leq 1$,[21] and for $CFL_m^+ = 1/2$. For this particular value of CFL_m^+, Eq. (29) with $\kappa = 0$ gives the constraints on $\phi_{m,\ell}^{\pm}$ for explicit schemes.[22,23] A comparison of Eq. (29) for $\kappa = 1$ and for $\kappa = 0$ shows that the TVD bounds on $\phi_{m,\ell}^{\pm}$ are tighter for implicit than for explicit TVD schemes. In the actual computations with the implicit ($\kappa = 1$) schemes, $\phi_{m,\ell}^{\pm}$ is chosen to be

$$\phi_{m,\ell}^{\pm} = \max[0, \min(1, r_{m,\ell}^{\pm}, \kappa \cdot 2r_{m,\ell\pm1}^{\mp})] \tag{30}$$

which for $\kappa = 0$ is equivalent to a min-mod limiter.[21,22] This limiter gives up to third-order-accurate differences for $0 \leq r_{\mathrm{m},\ell}^{\pm} \leq 1$ and $\lambda_m \gtrless 0$. When the min-mod part in Eq. (30) is replaced with Roe's superbee limiter,[24] this is also achieved, but for $1 \leq r_{m,\ell}^{\pm} \leq 2r_{m,\ell\pm1}^{\mp}$ and $\lambda_m \gtrless 0$, which in practice turns out to be a smaller range. Therefore, the attainable resolution is slightly better with Eq. (30) than with the superbee equivalent for Eq. (30). Van Leer derived various differentiable limiters,[18,23] which always interpolate in the convex region between $\phi_{m,\ell}^{\pm} = r_{m,\ell}^{\pm}$ and $\phi_{m,\ell}^{\pm} = 1$,[22] thus leading to, at most, second-order accuracy. A variant of Eq. (30) for $\kappa = 0$ as proposed by Osher and Chakravarthy[21] was found to be less efficient since it lacks Sweby's symmetry property[22] in the neighborhood of $r_{m,\ell}^{\pm} = 1$.

The extension of the TVD scheme to nonlinear hyperbolic conservation laws is

$$\begin{aligned}[&(1/\tau J) - (\lambda_{m,\ell+\frac{1}{2}}^- \Delta_{\ell+\frac{1}{2}} - \lambda_{m,\ell-\frac{1}{2}}^+ \Delta_{\ell-\frac{1}{2}})^n] \Delta w_m^n \\ &= \{\lambda_{m,\ell+\frac{1}{2}}^- - [(1-\omega)\lambda_{m,\ell+\frac{1}{2}}^- + (1+\omega)\lambda_{m,\ell+\frac{1}{2}}^+] \\ &\times (\phi_{m,\ell+1}^- - \phi_{m,\ell}^+)/4\}^n \Delta_{\ell+\frac{1}{2}} w_m^n \\ &- \{\lambda_{m,\ell-\frac{1}{2}}^+ + [(1-\omega)\lambda_{m,\ell-\frac{1}{2}}^+ + (1+\omega)\lambda_{m,\ell-\frac{1}{2}}^-] \\ &\times (\phi_{m,\ell}^- - \phi_{m,\ell-1}^+)/4\}^n \Delta_{\ell-\frac{1}{2}} w_m^n \end{aligned} \tag{31}$$

Following a multiplication of Eq. (31) by the set of right eigenvectors $\boldsymbol{R}$ from the left, a conservative high-resolution scheme for the nonlinear system case is easily derived:

$$[(\boldsymbol{I}/\tau J) - (\boldsymbol{D}^{-}_{\ell+\frac{1}{2}}\Delta_{\ell+\frac{1}{2}} - \boldsymbol{D}^{+}_{\ell-\frac{1}{2}}\Delta_{\ell-\frac{1}{2}})^{n}]\Delta\boldsymbol{Q}^{n}$$
$$= (\boldsymbol{R}\boldsymbol{K}^{-}\boldsymbol{R}^{-1})^{n}_{\ell+\frac{1}{2}}\Delta_{\ell+\frac{1}{2}}\boldsymbol{Q}^{n} - (\boldsymbol{R}\boldsymbol{K}^{+}\boldsymbol{R}^{-1})^{n}_{\ell-\frac{1}{2}}\Delta_{\ell-\frac{1}{2}}\boldsymbol{Q}^{n} \quad (32)$$

with

$$\boldsymbol{K}^{\mp}_{\ell\pm\frac{1}{2}} = \pm\{\boldsymbol{\Lambda}^{\mp}_{\ell\pm\frac{1}{2}} - [(1-\omega)\boldsymbol{\Lambda}^{\mp}_{\ell\pm\frac{1}{2}} + (1+\omega)\boldsymbol{\Lambda}^{\pm}_{\ell\pm\frac{1}{2}}]$$
$$\times(\boldsymbol{\Phi}^{\mp}_{\ell\pm1} - \boldsymbol{\Phi}^{\pm}_{\ell})/4\}^{n}$$

$$\boldsymbol{\Phi}^{\pm}_{\ell} = \mathrm{diag}(\phi_1^{\pm},\phi_2^{\pm},\phi_3^{\pm},\phi_4^{\pm})_{\ell}$$

Discretization of the Viscous Fluxes

The viscous flux terms are formed by first expanding the Cartesian derivatives in Eq. (3) via chain rule. Whenever possible, the derivatives at the cell interfaces are approximated like

$$(u_{\xi})_{j+\frac{1}{2}} = \Delta_{j+\frac{1}{2}}u, \text{ etc.} \quad (33)$$

Otherwise, they are computed from an arithmetic average of their central differences at the two nearest neighboring points; for instance,

$$(u_{\xi})_{i+\frac{1}{2}} = [(u_{j+1}-u_{j-1})_{i+1} + (u_{j+1}-u_{j-1})_{i}]/4 \quad (34)$$

The viscous shear fluxes required all nine metric coefficients at each of the six bounding surfaces of every computational cell. A source-free differencing of the metrics such as in Eq. (21) can only be devised for the three metric quantities that are needed for the inviscid flux terms. Whenever one of the remaining six metric coefficients is required (i.e., for the differencing of the cross-derivative terms), it is expressed by its centroidal value. It can be proven by simple but lengthy algebra that this approach maintains shear flows with constant gradients.

IV. Time Differencing

A first-order, Euler backward-time differencing for the three-dimensional Navier-Stokes equations is given by

$$[(\boldsymbol{I}/\tau J) - (\boldsymbol{A}^{-}+\boldsymbol{X})_{i+\frac{1}{2}}\Delta_{i+\frac{1}{2}} + (\boldsymbol{A}^{+}+\boldsymbol{X})_{i-\frac{1}{2}}\Delta_{i-\frac{1}{2}}$$
$$-(\boldsymbol{B}^{-}+\boldsymbol{Y})_{j+\frac{1}{2}}\Delta_{j+\frac{1}{2}} + (\boldsymbol{B}^{+}+\boldsymbol{Y})_{j-\frac{1}{2}}\Delta_{j-1\frac{1}{2}}$$
$$-(\boldsymbol{C}^{-}+\boldsymbol{Z})_{k+\frac{1}{2}}\Delta_{k+\frac{1}{2}}$$
$$+(\boldsymbol{C}^{+}+\boldsymbol{Z})_{k-\frac{1}{2}}\Delta_{k-\frac{1}{2}}]^{n}\Delta\boldsymbol{Q}^{n} = -\mathrm{RES}(\boldsymbol{Q}^{n}) \quad (35)$$

The algorithm is cast in delta form to compute steady-state solutions that are independent from the time-step size.[10] The residual RES $(\boldsymbol{Q}^{n})$ is the discrete representation of the spatial derivatives in Eq. (5) evaluated at time level n, applying the high-resolution schemes to the inviscid fluxes and central differencing to the shear flux terms. Equation (35) is solved by an implicit hybrid algorithm, where a symmetic planar Gauss-Seidel relaxation is used in the ζ direction and approximate factorization in the ξ and η direction:

$$[\boldsymbol{M} - (\boldsymbol{B}^{-}+\boldsymbol{Y})_{j+\frac{1}{2}}\Delta_{j+\frac{1}{2}} + (\boldsymbol{B}^{+}+\boldsymbol{Y})_{j-\frac{1}{2}}\Delta_{j-\frac{1}{2}}]\Delta\tilde{\boldsymbol{Q}}$$
$$= -\mathrm{RES}(\boldsymbol{Q}^{n},\boldsymbol{Q}^{n+1}) \quad (36a)$$

$$[\boldsymbol{M} - (\boldsymbol{C}^{-}+\boldsymbol{Z})_{k+\frac{1}{2}}\Delta_{k+\frac{1}{2}}$$
$$+(\boldsymbol{C}^{+}+\boldsymbol{Z})_{k-\frac{1}{2}}\Delta_{k-\frac{1}{2}}]^{n}\Delta\tilde{\boldsymbol{Q}}^{n} = \boldsymbol{M}\Delta\boldsymbol{Q} \quad (36b)$$

$$\boldsymbol{Q}^{n+1} = \boldsymbol{Q}^{n} + \Delta\boldsymbol{Q}^{n} \quad (36c)$$

with $\boldsymbol{M} = \boldsymbol{I}/\tau\boldsymbol{J} + (\boldsymbol{A}^{-}+\boldsymbol{X})_{i+\frac{1}{2}} + (\boldsymbol{A}^{+}+\boldsymbol{X})_{i-\frac{1}{2}}$, where $\mathrm{RES}(\boldsymbol{Q}^{n},\boldsymbol{Q}^{n+1})$ indicates the nonlinear updating of the residual while sweeping in the ζ direction back and forth through the computational domain. After each single sweep, the solution $\boldsymbol{Q}$ is updated for the time level $n+1$. The hybrid algorithm avoids the τ^3 spatial splitting error incurred by three-dimensional AF algorithms, which imposes a severe time-step limitation. Like relaxation methods, the hybrid algorithm is unconditionally stable for linear systems, but it additionally offers the advantage of being vectorizable.

V. Computational Integration Domain

The outer contour of the finite, three-dimensional integration domain around a sharp-edged delta wing (AR = 1, $t/c = 0$) is described by a half-hemispherical cylinder with the radius $R/c = 2$. The H-C-type grids used in the computations reported below extend from one root chord upsteam of the apex to about 1.7 root chords aft of the trailing edge. This integration domain is sliced into 72 cross planes perpendicular to the longitudinal axis of the delta wing, with some clustering in the apex and in the trailing-edge region (minimum spacing: 0.625×10^{-2} root chords) and exponential stretching in the wake region. In these cross planes, C-type grids are generated from solutions to elliptic systems.[25] The coarse and the medium grids have 51 grid points in both the circumferential (ξ) and radial (η) directions. Both grids have the same spacing in circumferential direction. A stronger coordinate stretching in the η direction for the medium grid than for the coarse grid gives a finer resolution of the boundary-layer-type flow along with wing surface. This is reflected by a maximum spacing in the η direction between the wing surface and the first η-const plane encompassing the wing, which is 0.14×10^{-2} and 0.25×10^{-3} root chords for the coarse and the medium grid, respectively. The standard grid with 101×51 grid points has the same spacing as the medium grid in radial direction but has twice as fine a resolution in circumferential direction. Additionally, a fine grid with 65×129 grid points in each ζ = const plane has been used. Computations on that fine grid proved that the solutions on the standard grid are spatially fully converged.

To assess the effect of the position of the outflow cross plane on the flow over the wing, the integration domain was expanded or shortened in the longitudinal direction by inserting or taking out cross planes.

VI. Boundary Conditions

Unknown values of $\boldsymbol{Q}$ on the boundaries are updated explicitly, and $\Delta\boldsymbol{Q}^{n}$ is set to zero. The explicit treatment of the boundaries lead to a more flexible scheme, where the boundary conditions become a modular element that can be plugged in or pulled out of a computer program without disturbing the implicit algorithm.

The boundary conditions consist of freestream conditions on the outer boundary, except for the outflow cross section, reflection conditions along the symmetry plane perpendicular to the wing, and no-slip conditions along the wing surface. For the computation of the pressure on the wing, the normal gradient of p is assumed to be zero. Flowfield values along the branch cut in the wake region are found by averaging the extrapolates of the dependent variables from above and below. The values of $\boldsymbol{Q}$ along the outflow cross section are computed from first-order extrapolation. The position of the outflow boundary was varied in the range between one and three root chords downstream of the trailing edge, without finding any discernable differences in the pressure and velocity distribution over the wing.

The values of the limiters $\phi^{\pm}_{m,\ell}$ along all boundaries are set to zero, corresponding to a zeroth-order extrapolation. The initial conditions consist of the freestream values.

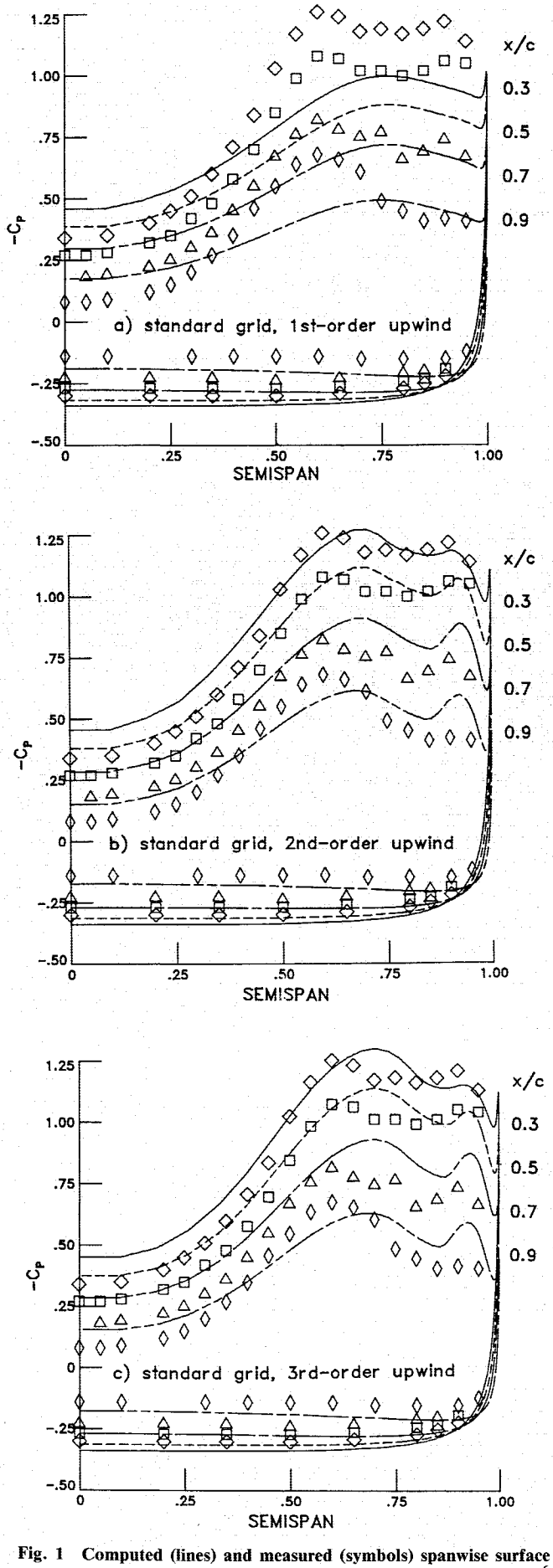

Fig. 1 Computed (lines) and measured (symbols) spanwise surface pressure coefficient distributions, $AR=1$, $\alpha=20.5$ deg, $Re=0.9\times10^6$ (laminar flow).

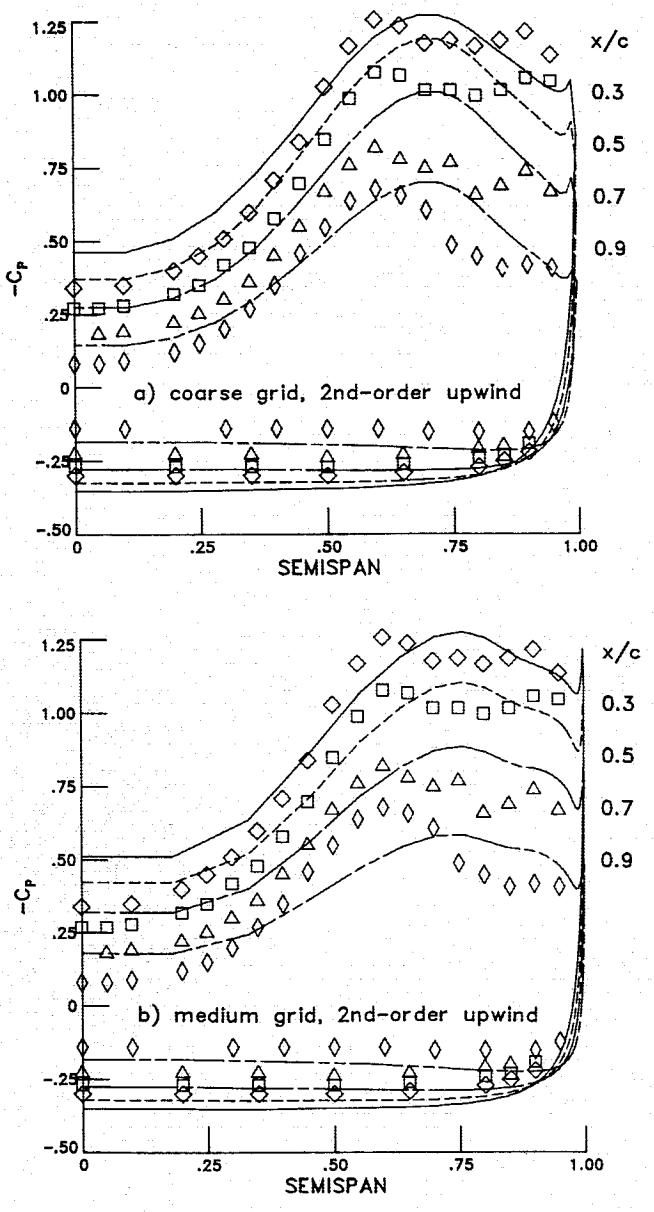

Fig. 2 Effect of grid refinement, $AR=1$, $\alpha=20.5$ deg, $Re=0.9\times10^6$ (laminar flow).

VII. Results

Viscous ($Re=0.9\times10^6$), vortical flows around a sharp-edged delta wing ($AR=1$, $t/c=0$) are computed as steady-state solutions to the incompressible Navier-Stokes equations.

The surface pressure distributions in Fig. 1 show comparisons between experimental data by Hummel for a similar wing[26] and three sets of computational results. The angle of attack is 20.5 deg, and the comparison is made for four root-chord stations: $x/c=0.3$, 0.5, 0.7, and 0.9. The computations are done on the standard grid for fully laminar flow, with the accuracy of the upwind differencing restricted to at most first order (Fig. 1a), second order (Fig. 1b), and third order (Fig. 1c). The results in Fig. 1b are computed with $\omega=1$. Other choices of ω (i.e., $\omega=0$, $-1/3$, $1/2$, 1),[21] which make the upwind differences also accurate up to second order, do not significantly affect the flowfield results.

The first-order-accurate results are obviously swamped with numerical dissipation: neither the position nor the strength of the primary and secondary vortices are prediced properly at any root-chord station. Crossflow velocity vector plots (not shown here) demonstrate that there is a weak secondary vortex in the first-order-accurate calculations,[13] and secondary and

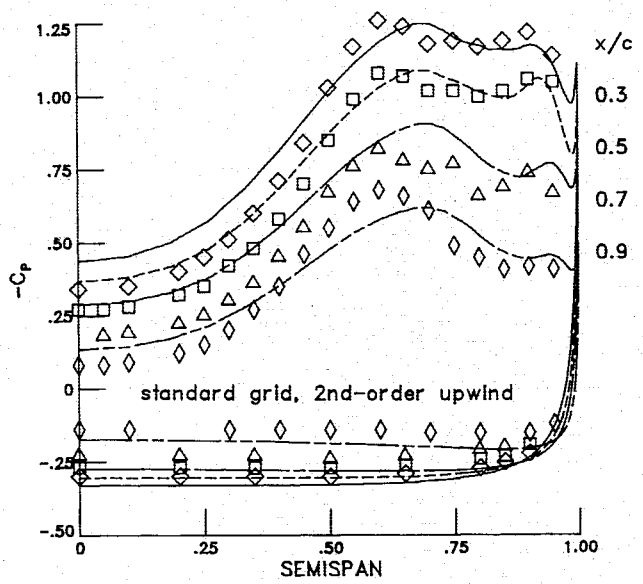

Fig. 3 Effect of turbulence modeling, $AR=1$, $\alpha=20.5$ deg, $Re=0.9\times10^6$.

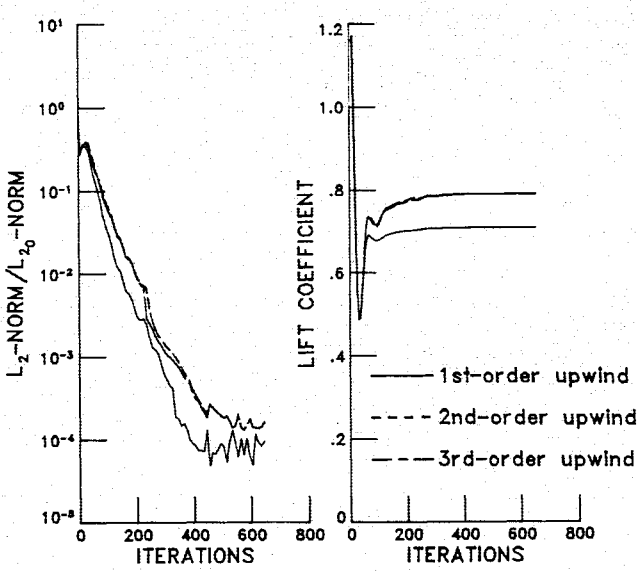

Fig. 4 Convergence summary for standard grid calculations, $AR=1$, $\alpha=20.5$ deg, $Re=0.9\times10^6$ (laminar flow).

tertiary vortices in the flowfield results computed with the up to second- and third-order-accurate upwind differencing.

The effect of the secondary vortex on the pressure distribution is clearly seen in the experiment and in the computations with the up to second- and third-order-accurate upwind differences. Because of the central differencing of the shear fluxes, the schemes are at most second-order accurate, no matter how accurate the upwinding is. Consequently, the results in Figs. 1b and 1c differ only marginally.

The effects of grid refinement on the spanwise surface pressure distribution are shown in Fig. 2. The primary vortex in Fig. 2a is predicted in acceptable agreement with the corresponding standard grid result in Fig. 1b, but the secondary and tertiary vortices are not captured at all. This reveals that a strong clustering of coordinate surfaces enveloping the delta wing is essential to mimic the physics of the viscous flow along the wing surface.

In order to assess the effect of a thin-layer approximation to the Navier-Stokes equations on the computed flowfield results, the present computations were repeated with the viscous shear fluxes retained only in η direction. These results

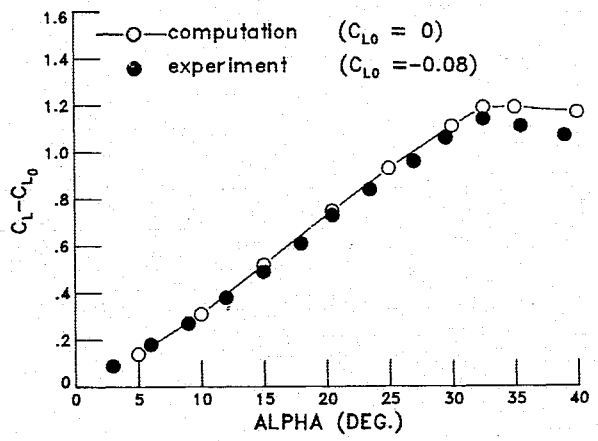

Fig. 5 Variation of lift with angle of attack, $AR=1$, $Re=0.9\times10^6$ (laminar flow).

are identical within plotting accuracy with those in Figs. 1 and 2. Computing viscous vortex flows as solutions to the Navier-Stokes equations in their thin-layer approximation bears the advantage that the effects of turbulence can be easily accounted for through the use of the two-layer, zero equation model by Baldwin and Lomax,[27] with the modifications for flows with massive separation as suggested by Degani and Schiff.[28] The effectiveness of this approach and the necessity to include a turbulence modeling capability is demonstrated by the computed spanwise surface pressure distributions in Fig. 3, which are calculated for transitional flow. The transitional flow is simulated by assuming laminar flow along the windward wing surface and by fixing the laminar/turbulent transition on the leeward side at $x/c=0.6$. The effect of turbulence is clearly seen for $x/c>0.7$; the fully laminar calculation (Fig. 1b) considerably overpredicts the strength of the secondary vortex, whereas the calculation with transition modeling brings the pressure distribution in closer agreement with the experimental data.

Figure 4 documents the efficiency of the high-resolution schemes for the $\alpha=20.5$ deg case. All computations are carried out in half-precision arithmetic (i.e., seven significant decimal places) on the CDC Cyber 205 vector computer at NASA Ames Research Center. With the high-resolution schemes, the normalized L_2 norm of all residuals is driven to machine zero with a spectral radius of 0.980 (0.977 for the first-order-accurate scheme). The L_2 norms are scaled with the L_2 norm after the first complete sweep in the ζ direction through the integration domain, which is about 10^{-2}. The parameter β is set to unity, and local time stepping is used with a Courant-Friedrichs-Lewy (CFL) number of 10. The central processor unit (CPU) time per grid point and per iteration is 27.2 μs for the first-order-accurate scheme, and 37.4 μs for the high-resolution schemes, regardless what value for the parameter ω is chosen. Solving the Navier-Stokes equations in their thin-layer approximation saves about 2% off these CPU-time values.

The high-resolution schemes sustained this convergence performance for all standard grid computations shown in Fig. 5 with unchanged values for β and CFL. Figure 5 displays the variation of lift with increased angle of attack. As long as the lift is linear, the computed lift is systematically higher than the measured lift due to the different wing geometries: the cambered wind-tunnel model produces negative lift at 0 angle of attack. The differences in the computed and in the measured nonlinear lift are attributed to the fact that in the computations the flow is assumed to be fully laminar, whereas in the experiment a laminar/turbulent transition seems to occur (cf., measured and calculated loads in Fig. 3 and their discussion). The maximum lift is predicted at the same angle of attack as in the experiment[26] whereas the peak in lift is

associated with the onset of a vortex burst at the trailing edge. Inspection of the computed flowfield for $\alpha = 32.5$ deg reveals that a bubble-type vortex breakdown close to the trailing edge is computed as a steady-state solution to the Navier-Stoke equations.

VIII. Conclusions

Based on flux-difference splitting, implicit high-resolution schemes have been constructed for efficient calculations of steady-state solutions to the three-dimensional, incompressible Navier-Stokes equations in curvilinear coordinates. The upwind differencing of the inviscid fluxes can be made up to third-order-accurate by a linear reconstruction of the solution from its cell averages. The reconstruction process itself is nonlinear, since it selects node stencils such that it gives high resolution in regions of a smooth solution, while it suppresses oscillations in regions where the solution undergoes rapid changes in gradient. The reconstruction algorithm is derived from one used in recently developed implicit TVD schemes. The viscous shear fluxes are centrally differenced with second-order accuracy. The implicit hybrid algorithm uses approximate factorization in crossflow planes, while it resembles a symmetric planar Gauss-Seidel relaxation by sweeping back and forth in the remaining coordinate direction, nonlinearly updating the residual. The computed vortical flows around a sharp-edged delta wing agree quite well with experimental data for a similar delta wing. Even flows with a vortex burst are computable, as demonstrated by the variation of lift with increased angle of attack. The high-resolution schemes proved to be efficient for all test cases in which they sustained their fairly good convergence performance reflected by a spectral radius of about 0.980.

Acknowledgement

NASA Langley sponsored the work of the authors under Contract NAS 1-17919, awarded to Vigyan Research Associates, Inc., Hampton, VA.

References

[1]Vatsa, V.N., "Accurate Solutions for Transonic Viscous Flow Over Finite Wings," *Journal of Aircraft,* Vol. 24, June 1987, pp. 377–385.

[2]Pulliam, T.H. and Steger J.L., "On Implicit Finite-Difference Solutions of Three-Dimensional Flow," AIAA Paper 78-10, Jan. 1978.

[3]Obayashi, S. and Fujii, K., "Computation of Three-Dimensional Viscous Transonic Flows with the LU Factored Scheme," AIAA Paper 85-1510, July 1985.

[4]Thomas, J.L., Taylor, S.L., and Anderson, W.K., "Navier-Stokes Computations of Vortical Flows Over Low Aspect Ratio Wings," AIAA Paper 87-0207, Jan. 1987.

[5]Steger, J.L. and Kutler, P., "Implicit Finite-Difference Procedures for the Computation of Vortex Wakes," *AIAA Journal,* Vol. 15, April 1977, pp. 581–590.

[6]Aziz, K. and Hellums, J.D., "Numerical Solution of the Three-Dimensional Equations of Motion for Laminar Natural Convection," *Physics of Fluids,* Vol. 10, Feb. 1967, pp. 314–324.

[7]Harlow, F.H. and Welch, J.D., "Numerical Calculation of Time-Dependent Viscous Incompressible Flow of Fluid with Free Surface," *Physics of Fluids,* Vol. 8, Dec. 1965, pp. 2182–2189.

[8]Hartwich, P.-M., "Finite Difference Solutions of the Euler Equations in the Vicinity of Sharp Edges," *AIAA Journal,* Vol. 23, Nov. 1985, pp. 1820–1822.

[9]Chorin, A.J., "A Numerical Method for Solving Incompressible Viscous Flow Problems," *Journal of Computational Physics,* Vol. 2, No. 1, Aug. 1967, pp. 12–26.

[10]Warming, R.F. and Beam, R.M., "On the Construction and Application of Implicit Factored Schemes for Conservation Laws," *SIAM-AMS Proceedings,* Vol. 11, Society for Industrial and Applied Mathematics, Philadelphia, PA, 1978, pp. 85–129.

[11]Rizzi, A. and Eriksson, L.E., "Computation of Inviscid Incompressible Flow with Rotation," *Journal of Fluid Mechanics,* Vol. 49, March 1985, pp. 327–393.

[12]Steger, J.L. and Warming, R.F., "Flux Vector Splitting of the Inviscid Gasdynamics Equations with Application to Finite-Difference Methods," *Journal of Computational Physics,* Vol. 40, No. 2, April 1981, pp. 263–293.

[13]Hartwich, P.-M., Hsu, C.-H., and Liu, C.H., "Implicit Hybrid Schemes for the Flux-Difference Split, Three-Dimensional Navier-Stokes Equations," *Lecture Notes in Physics,* Vol. 264, Springer-Verlag, New York, 1986, pp. 303–307.

[14]Roe, P.L., "Approximate Riemann Solves, Parameter Vectors, and Difference Schemes," *Journal of Computational Physics,* Vol. 43, No. 2, Oct. 1981, pp. 357–372.

[15]Van Leer, B., "Flux Vector Splitting for the Euler Equations," *Lecture Notes in Physics,* Vol. 170, Springer-Verlag, New York, 1982, pp. 507–512.

[16]Chakravarthy, S.R., Anderson, D.A., and Salas, M.D., "The Split Coefficient Matrix Method for Hyperbolic Systems of Gasdynamics Equations," AIAA Paper 80-0268, Jan. 1980.

[17]Lax, P.D., *Hyperbolic Systems of Conservation Laws and the Mathematical Theory of Shock Waves,* SIAM, Philadelphia, PA, 1972.

[18]Van Leer, B., "Towards the Ultimate Conservative Difference Scheme, IV. A New Approach to Numerical Convection," *Journal of Computational Physics,* Vol. 23, No. 3, March 1977, pp. 276–299.

[19]Harten, A., "High Resolution Schemes for Hyperbolic Conservation Laws," *Journal of Computational Physics,* Vol. 49, No. 3, March 1983, pp. 357–393.

[20]Yee, H.C., Warming, R.F., and Harten, A., "Implicit Total Variation Diminishing (TVD) Schemes for Steady-State Calculations," *Journal of Computational Physics,* Vol. 57, No. 3, March 1985, pp. 327–360.

[21]Osher, S. and Chakravarthy, S.R., "Very High Order Accurate TVD Schemes," ICASE Rept. 84-44, Sept. 1984.

[22]Sweby, P.K., "High Resolution Upwind Schemes Using Flux Limiters for Hyperbolic Conservation Laws," *SIAM Journal on Numerical Analysis,* Vol. 21, No. 5, Oct. 1984, pp. 995–1011.

[23]Van Leer, B., "Towards the Ultimate Conservative Difference Scheme, II. Monotonicity and Conservation Combined in a Second-Order Scheme," *Journal of Computational Physics,* Vol. 14, No. 4, April 1974, pp. 361–370.

[24]Roe, P.L., "Some Contributions to the Modelling of Discontinuous Flows," *Lectures in Applied Mathematics,* Vol. 22, American Mathematical Society, Providence, RI, 1985, pp. 163–193.

[25]Hartwich, P.-M., "Three-Dimensional Grids as Solutions of Elliptic Systems," AIAA Paper 86-0430, Jan. 1986.

[26]Hummel, D., "On the Vortex Formation Over a Slender Delta Wing at Large Angles of Incidence," AGARD-CP-247, Paper No. 15, 1978.

[27]Baldwin, B.S. and Lomax, H., "Thin Layer Approximation and Algebraic Model for Separated Turbulent Flows," AIAA Paper 78-257, Jan. 1978.

[28]Degani, D. and Schiff, L.B., "Computation of Turbulent Supersonic Flows Around Pointed Bodies Having Crossflow Separation," *Journal of Computational Physics,* Vol. 66, No. 1, Sept. 1986, pp. 173–196.